

# Catalytic Effect on CO<sub>2</sub> Electoreduction by Hydroxyl Terminated Two-Dimensional MXenes

*Hetian Chen,<sup>1</sup> Albertus D. Handoko,<sup>2</sup> Jiewen Xiao,<sup>1</sup> Xiang Feng,<sup>1</sup> Yanchen Fan,<sup>1</sup>*

*Tianshuai Wang,<sup>1</sup> Dominik Legut,<sup>3</sup> Zhi Wei Seh,<sup>\*,2</sup> and Qianfan Zhang<sup>\*,1</sup>*

*<sup>1</sup> School of Materials Science and Engineering, Beihang University, Beijing, 100191, P. R. China.*

*<sup>2</sup> Institute of Materials Research and Engineering, Agency for Science, Technology and Research (A\*STAR), 2 Fusionopolis Way, Innovis, Singapore 138634, Singapore.*

*<sup>3</sup> IT4Innovations Center, VSB-Technical University of Ostrava, 17. listopadu 15, CZ-708 33 Ostrava, Czech Republic.*

## ABSTRACT

Electrocatalysis represents a promising method to generate renewable fuels and chemical feedstock from the carbon dioxide reduction reaction (CO<sub>2</sub>RR). However, traditional electrocatalysts based on transition metals are not efficient enough because of the high overpotential and slow turnover. MXenes, a family of two-dimensional metal carbides and nitrides, have been predicted to be effective in catalyzing CO<sub>2</sub>RR, but a systematic investigation into their catalytic performance is lacking, especially on hydroxyl (–OH) terminated MXenes relevant in aqueous reaction conditions. In this work, we utilized first-principles simulations to systematically screen and explore the properties of MXenes in catalyzing CO<sub>2</sub>RR to CH<sub>4</sub> from both aspects of

thermodynamics and kinetics.  $\text{Sc}_2\text{C}(\text{OH})_2$  was found to be the most promising catalyst with the least negative limiting potential of -0.53 V vs. RHE. This was achieved through an alternative reaction pathway, where the adsorbed species are stabilized by capturing H atom from the MXene's OH-termination group. New scaling relations, based on the shared H interaction between intermediates and MXenes, were established. Bader charge analyses reveal that catalysts with less electron migration in the  $^*(\text{H})\text{COOH} \rightarrow ^*\text{CO}$  elementary step exhibit better  $\text{CO}_2\text{RR}$  performance. This study provides new insights regarding the effect of surface functionalization on the catalytic performance of MXenes to guide future materials design.

**KEYWORDS:**  $\text{CO}_2$  reduction reaction, two-dimensional materials, OH-terminated MXene, first-principle simulation, scaling relationship

## INTRODUCTION

Due to its persistence in the atmosphere,  $\text{CO}_2$  is considered as one of the main contributors to global climate change. As the majority of anthropogenic  $\text{CO}_2$  emission originates from fossil fuel combustion, efforts in mitigating  $\text{CO}_2$  emission relies on the continued push towards the use of cleaner sources of fuel, including renewable energy.<sup>1</sup> In this regard, electrocatalytic  $\text{CO}_2$  reduction reaction ( $\text{CO}_2\text{RR}$ ), especially when coupled with renewable electricity, is an attractive solution that enables utilization of  $\text{CO}_2$  into valuable chemicals and fuels.<sup>2-9</sup> Despite the widespread attention, there are still significant challenges that need to be surmounted before large-scale industrial  $\text{CO}_2\text{RR}$  can be realized. In particular, the lack of low cost electrocatalysts with high

activity, selectivity and durability remains the critical issue in this field.<sup>10-12</sup> Copper metal, one of the benchmark heterogeneous catalysts to facilitate the CO<sub>2</sub>RR process, is still unsatisfactory due to the large CO<sub>2</sub>RR overpotential and low selectivity towards a particular product.<sup>13-22</sup> Among the diverse CO<sub>2</sub>RR products on Cu catalyst, CH<sub>4</sub> starts to form at potentials more negative than -0.9 V (all potentials in this work is expressed vs. reversible hydrogen electrode, RHE), but with slow reaction kinetics.<sup>23, 24</sup> If a relatively decent partial current density (*e.g.* 5-10 mA cm<sup>-2</sup>) is required, potentials more negative than -1.1 V are required.<sup>16, 24</sup> Therefore, discovering a suitable new catalyst that can reduce the reaction overpotentials is crucial for practical CO<sub>2</sub>RR applications.

MXenes are a relatively new family of 2D transition metal carbides and nitrides with the chemical formula  $M_{n+1}X_nT_x$  ( $n = 1-3$ ; M = early transition metal; X = C and/or N; T<sub>x</sub> = surface terminations), obtained by etching the respective MAX phases.<sup>25-29</sup> There are many excellent properties of MXenes, making them one of the most appealing 2D systems for energy storage, including supercapacitors and batteries.<sup>30</sup> MXenes are chemically and mechanically stable, which enables a wide array of applications in real-life environment. Furthermore, the electronic structure of MXenes can be modified by tuning the number of valence electrons, which can be realized by synthesizing MXenes with different transition metals.<sup>31</sup> The high surface area, tunable surface groups and multiple binding sites of MXenes also render them promising as electrocatalysts for energy conversion reactions.<sup>32</sup> In previous work, it has been demonstrated that high activity for hydrogen evolution reaction (HER) on MXenes can be achieved by carefully tuning the surface species and terminations.<sup>33-37</sup> Therefore,

promising catalytic activity for CO<sub>2</sub>RR on MXenes may also be expected with appropriate surface modification.

There have been some works focusing on MXenes' catalytic effect in CO<sub>2</sub>RR. Zhang *et al.* investigated the CO<sub>2</sub>RR activity on 3 types of MXenes, Ti<sub>2</sub>CO<sub>2</sub>, V<sub>2</sub>CO<sub>2</sub> and Ti<sub>3</sub>C<sub>2</sub>O<sub>2</sub> by means of density functional theory (DFT) computations, and suggested that Ti<sub>2</sub>CO<sub>2</sub> can be a promising photocatalyst for CO<sub>2</sub> reduction.<sup>38</sup> Li *et al.* studied 8 different bare MXenes with formula M<sub>3</sub>C<sub>2</sub> (without surface termination), and found that Cr<sub>3</sub>C<sub>2</sub> and Mo<sub>3</sub>C<sub>2</sub> exhibit the most promising CO<sub>2</sub> to CH<sub>4</sub> conversion capabilities.<sup>39</sup> Handoko *et al.* did a more comprehensive work on 19 kinds of O-terminated MXenes, discovering the least negative CO<sub>2</sub>RR limiting potential for Ti<sub>2</sub>CO<sub>2</sub> and W<sub>2</sub>CO<sub>2</sub> (-0.52 and -0.35 V respectively).<sup>34</sup> Although encouraging progress has been made, we note that investigation into hydroxyl (-OH) terminated MXenes, the likely form in direct contact with aqueous solutions,<sup>40</sup> is lacking. Further systematic study is therefore required to clarify and understand the CO<sub>2</sub>RR mechanism in -OH terminated MXenes.

In this present work, we utilize the first-principles approach to systematically explore CO<sub>2</sub>RR properties on 17 different MXenes with -OH termination groups from both aspects of thermodynamics and kinetics.<sup>41</sup> It is found that the adsorption of intermediates differs considerably on various -OH terminated MXenes. Among them, Sc<sub>2</sub>C(OH)<sub>2</sub> and Y<sub>2</sub>C(OH)<sub>2</sub> possess the least negative CO<sub>2</sub>RR limiting potential of -0.53 and -0.61 V respectively. At the same time, the competing HER was disfavored due to strong -H binding. We believe such effects are closely related to the high reactivity of H in the -OH termination groups of MXenes. Further electronic structure analysis

demonstrated that MXene catalysts with less charge migration during the elementary step can induce higher catalytic activity. This work systematically reveals the catalytic properties of OH-terminated MXenes during CO<sub>2</sub>RR, and at the same time, provides new insights on the effect of surface functionalization in optimizing the catalytic performance of MXenes.

## METHOD

Density functional theory (DFT) based first-principles schemes were carried out for our simulation. The project augmented wave (PAW) and the Perdew-Burker-Ernzerhof (PBE) was chosen. Both RPBE and vdw-DF2 functional were also used to benchmark the calculation in this study, resulting in similar simulation result especially for the key potential-limiting step (see detail in Supporting Information). A cutoff energy 400 eV was applied for all works. The Brillouin zone was sampled by a Monkhorst-Pack  $3\times3\times1$   $k$ -point grid for the  $3\times3\times1$  supercell. At least 20 Å of vacuum in the  $z$ -direction was used to separate the slab in order to avoid the artificial interaction among the periodic units. Structures were relaxed until the force on each atom was less than 0.01 eV Å<sup>-1</sup>.

Here, we refer to the computational hydrogen electrode (CHE) model<sup>42</sup> in calculating the reaction limiting potential. The limiting potentials of elementary hydrogenation reactions are defined as the potential at which the reaction becomes exergonic (downhill in free energy). As for a specific reaction, the free energy change of the reaction will be:

$$\begin{aligned}\Delta G_{elem} &= \mu(B *) - \mu(A *) - [\mu(H^+) + \mu(e^-)] \\ &= \mu(B *) - \mu(A *) - [\frac{1}{2}\mu(H_{2(g)}) - eU]\end{aligned}$$

As the  $\Delta G_{elem} = 0$  at  $U = U_L$ , the limiting potential can be calculated using the following formula:

$$U_L = -\frac{\mu(B *) - \mu(A *) - \frac{1}{2}\mu(H_{2(g)})}{e} = \frac{-\Delta G_{elem}^{0V}}{e}$$

In this formula,  $\mu$  is the chemical potential of adsorbed species, which is calculated by the following equation:

$$\mu = E_{elec} + ZPE + \int C_p dT - T \times S$$

where the chemical potential is the summation of the calculated electronic energy ( $E_{elec}$ ), zero-point energy ( $ZPE$ ), heat capacity ( $C_p$ ) and entropy contribution ( $T \times S$ ). Zero-point energies, heat capacities and entropies are calculated from vibrations states by standard methods.<sup>43</sup> In addition, the harmonic oscillator approximation is applied for all the calculation of the vibration properties. The temperature ( $T$ ) is assumed to be 298.15 K to simulate the room temperature condition.<sup>44, 45</sup> The reaction free energy of each intermediate state  $G_C$  can be expressed as the sum of the free energy change of all the reaction before the formation of the specified intermediate states

$$G_C = \sum_{CO_2}^C \Delta G_{elem}$$

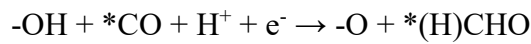
We assume that the reaction free energy of  $CO_2$  is zero, thus we can get the reaction free energy of all the intermediates.

## RESULTS AND DISCUSSION

Firstly, we investigated the layered structure and configuration of various –OH terminated MXenes. For bare MXenes, the typical conformations are illustrated in Supporting Figure S1(a), with the metal atoms located at the outermost layer. The stable geometry for –OH terminated MXenes varies depending on the types of transition metal elements (Supporting Table S1). A total of 17 different kinds of MXenes were investigated, namely:  $\text{Hf}_2\text{C}(\text{OH})_{2(fcc)}$ ,  $\text{Hf}_2\text{C}(\text{OH})_{2(hcp)}$ ,  $\text{Nb}_2\text{C}(\text{OH})_2$ ,  $\text{Sc}_2\text{C}(\text{OH})_2$ ,  $\text{Ta}_2\text{C}(\text{OH})_2$ ,  $\text{Ti}_2\text{C}(\text{OH})_2$ ,  $\text{V}_2\text{C}(\text{OH})_2$ ,  $\text{Y}_2\text{C}(\text{OH})_2$ ,  $\text{Zr}_2\text{C}(\text{OH})_{2(fcc)}$ ,  $\text{Zr}_2\text{C}(\text{OH})_{2(hcp)}$ ,  $\text{Hf}_2\text{N}(\text{OH})_2$ ,  $\text{Nb}_2\text{N}(\text{OH})_2$ ,  $\text{Sc}_2\text{N}(\text{OH})_2$ ,  $\text{Ta}_2\text{N}(\text{OH})_2$ ,  $\text{Ti}_2\text{N}(\text{OH})_2$ ,  $\text{Y}_2\text{N}(\text{OH})_2$  and  $\text{Zr}_2\text{N}(\text{OH})_2$ . Systematic geometry optimization reveals that the hydroxyl termination prefers to sit on the *fcc* site in most of the cases (Figure S1b). On the other hand,  $\text{Hf}_2\text{N}(\text{OH})_2$ ,  $\text{Nb}_2\text{N}(\text{OH})_2$ ,  $\text{Ta}_2\text{N}(\text{OH})_2$  and  $\text{Ta}_2\text{C}(\text{OH})_2$  prefers the *hcp* configuration (Figure S1c). Exceptions were found in  $\text{Hf}_2\text{C}(\text{OH})_2$  and  $\text{Zr}_2\text{C}(\text{OH})_2$ , where the hydroxyl termination is more likely to be located at the *fcc* site on one side and *hcp* site on the other, forming a mixed termination pattern (Figure S1d). To demonstrate that OH-terminated MXenes is a realistic surface state, we also calculated the favorable termination for all MXenes investigated in this work (supporting information Figure S2). The result shows that the hydroxyl group is stable and energetically preferred for many kinds of MXenes, especially when negative potentials are applied. We note that the catalysts identified with high  $\text{CO}_2\text{RR}$  activity in this work tend to have high hydroxyl coverage.

After determining the preferred configuration and hydroxyl coverage of –OH

termination groups on various MXenes, we proceeded to investigate their CO<sub>2</sub>RR catalytic activity. The reaction free energy  $G_C$  of different intermediates for different protonation stages from CO<sub>2</sub> to CH<sub>4</sub> are systematically computed, and the catalytic effect can be evaluated by the limiting potential during the whole reaction process. The reduction of CO<sub>2</sub> to CH<sub>4</sub> progresses through multi-stepped transfer of 8 proton-electron pairs, as shown for Sc<sub>2</sub>C(OH)<sub>2</sub> (Figure 1). Interestingly, we found that the most stable intermediate configuration is achieved through captured H atom from the MXene's T<sub>x</sub> group by some of the intermediates. For example, in the \*CO→\*(H)CHO elementary step calculated on Sc<sub>2</sub>C(OH)<sub>2</sub> surface, the \*(H)CHO intermediate was formed through the capture of H in the –OH termination group and simultaneous proton-coupled electron transfer (PCET) (Figure 1a). To distinguish the H obtained from –OH termination vs. PCET, we denote the former with a pair of parentheses, thus \*(H)CHO contains one captured (H) from –OH termination and one H from PCET. Slab-*n*H represents the catalyst surface with *n* hydrogen vacancy. This process can be described by the following formula:



Where the -OH and -O are the surface terminations, while \*CO and \*(H)CHO are the adsorbates (\*(H)CHO contains one captured (H) atom).

Similarly, we found that the H from the –OH termination group in Sc<sub>2</sub>C(OH)<sub>2</sub> can also be shared with \*COOH, \*O, and \*OH intermediates, forming \*(H)COOH, \*(H<sub>2</sub>)O, and \*(H)OH respectively (Figure 1a). For these intermediates, the temporarily captured hydrogen will return to the catalyst as the reaction progresses (marked as (H)). However,



for certain intermediates in the elementary steps:  $^*(\text{H})\text{CHO} \rightarrow ^*(\text{H})\text{OC}[\text{H}]\text{H}_2 \rightarrow ^*(\text{H}_2)\text{O} + \text{C}[\text{H}]\text{H}_3$ , the lowest energy is achieved when the captured hydrogen remains in the intermediate molecule (marked as [H], see Supporting Figure S3 for details). This means the adsorbate permanently captures this [H], consequently creating a hydrogen vacancy in the MXene  $\text{T}_x$ . The vacancy is recovered in the last step, where one final PCET donates H back to the catalyst. It can be expressed as  $-\text{O} + \text{H}^+ + \text{e}^- \rightarrow -\text{OH}$ , making the final state is the same as the initial state and a total of 8 proton-electron pairs transfer from  $\text{CO}_2$  to  $\text{CH}_4$ .

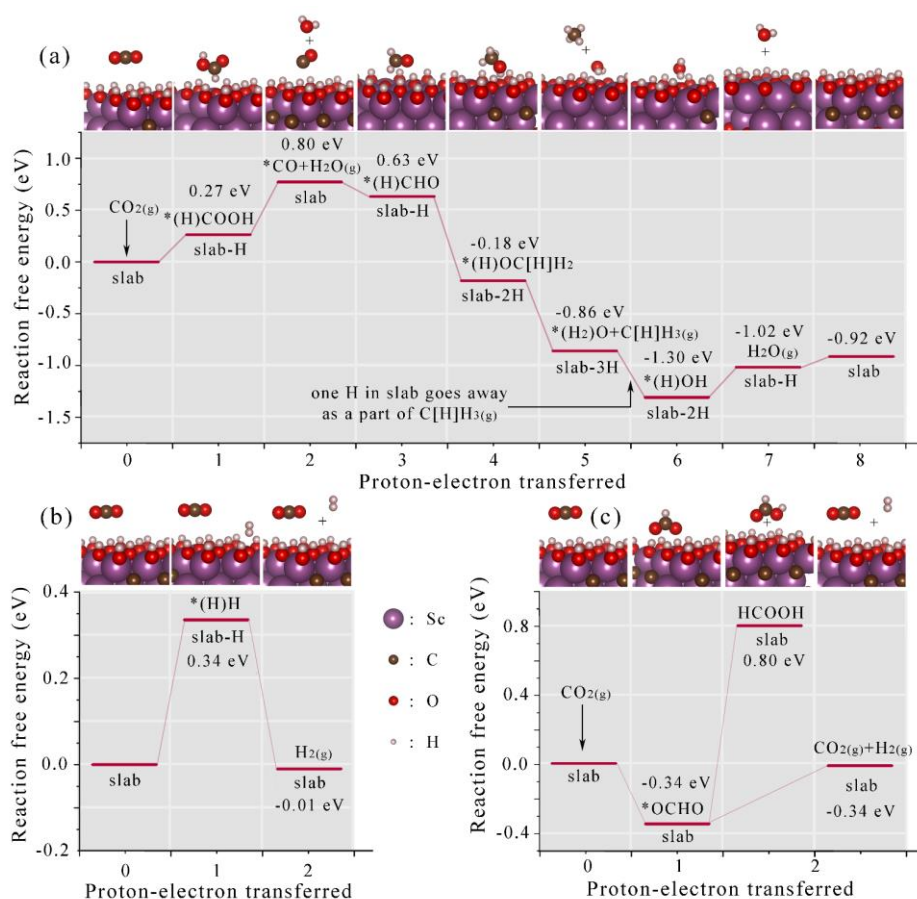


**Figure 1. Calculated free energy diagrams.** Free energy diagrams for the lowest energy pathways to (a)  $\text{CH}_4$ , (b)  $\text{H}_2$  and (c)  $\text{HCOOH}$  and  $\text{H}_2$  (through the  $^*\text{OCHO}$  intermediate) on  $\text{Sc}_2\text{C}(\text{OH})_2$ . The reaction free energy is calculated at 0 V vs. RHE. The (H) atoms are temporarily captured from

MXene's  $T_x$ , while [H] atoms indicate permanent capture. Slab- $nH$  represents the catalyst surface with  $n$  hydrogen vacancy. In (a), the (H) atom captured in the third PCET step of  $*CO \rightarrow *(H)CHO$  becomes permanently captured in the fourth PCET step of  $*(H)CHO \rightarrow *(H)OC[H]H_2$  (an additional (H) is captured in this step).

Theoretical calculations through this pathway reveal that  $Sc_2C(OH)_2$  and  $Y_2C(OH)_2$  are the most promising  $CO_2RR$  catalysts among all the MXenes studied here, with the least negative limiting potentials of -0.53 and -0.61 V, respectively (see Supporting Figure S4 for the free energy diagrams of all the MXenes). For many  $-OH$  terminated MXenes, it takes only a little energy to recover after the loss of hydrogen, thus the overpotential of the whole process can be reduced effectively.

We believe the distinct  $CO_2RR$  activity on  $-OH$  terminated MXenes can be attributed to the reactive H atom in the  $T_x$  group. To show this, we investigate the interaction between MXenes and key intermediates at the atomic level by computing the charge transfer between them and plotting the charge density difference during the adsorption of  $CO_2$ ,  $*(H)COOH$  and  $*(H)CHO$  (Figure 2 a-c). According to the adsorption conformations, the C atom in the intermediates are capable of binding the (H) atom in OH termination strongly, which can be seen from the significant electron migration from H to C. When  $CO_2$  adsorbs on catalyst, the charge around H atom in the  $-OH$  termination and O-H bond will migrate to the area between C and H (Figure 2a). As for  $*(H)COOH$  and  $*(H)CHO$ , the charge will transfer from O-H bond to C-H bond (Figure 2 b-c). It is therefore proposed that the H atom from the substrate possesses the ability to take part in the process of forming stable configuration with intermediates.

This is distinct from CO<sub>2</sub>RR process on transition metal surfaces, where most CO<sub>2</sub>RR intermediates bind to the substrate through –C coordination and three elementary steps, CO<sub>2</sub>→\*COOH, \*CO→\*COH and \*CO→\*CHO, tend to be potential-limiting.<sup>14, 15</sup> In –OH terminated MXene, the \*CHO group can transform into \*(H)CHO spontaneously by utilizing one hydrogen in the catalyst, while the \*COOH group can transform to \*(H)COOH by similar mechanism.

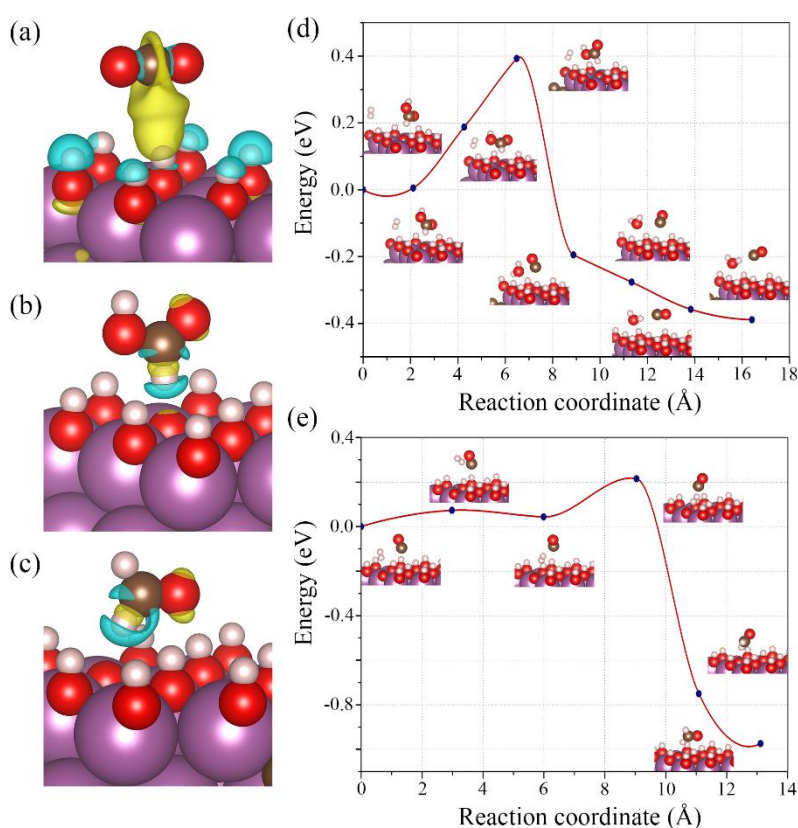


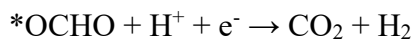
**Figure 2. Deformation charge density and energy barriers.** Deformation charge density of (a) CO<sub>2</sub>, (b) \*(H)COOH, (c) \*(H)CHO. Charge migrates from H and H-O bond to C-H bond. Charge flows out from blue areas and into the yellow areas. The interaction energy of fragments with substrate is -0.17 eV, -0.53 eV, -0.37 eV for CO<sub>2</sub>, (H)COOH and (H)CHO, respectively. The isodensity value plotted is 0.008 e/bohr<sup>3</sup> (0.054 e/Å<sup>3</sup>) for (H)COOH and (H)CHO, and 0.00007 e/bohr<sup>3</sup> (0.00047 e/Å<sup>3</sup>) for CO<sub>2</sub>. CI-NEB is used to find the transition state. Energy barriers along

the elementary step of (d)  $^*(\text{H})\text{COOH} \rightarrow ^*\text{CO}$ , (e)  $^*\text{CO} \rightarrow ^*(\text{H})\text{CHO}$ . In (d),  $^*(\text{H})\text{COOH} \rightarrow ^*\text{CO}$  is the potential-limiting step of the process. The barrier will affect the reaction speed to a great degree. In (e), there is no transition state like  $^*\text{CHO}$ .

Since HER is the primary competitive reaction to  $\text{CO}_2\text{RR}$ , we also considered the adsorption capacity for hydrogen atoms on different types of MXenes. Figure 1b shows the free energy diagram for HER on  $\text{Sc}_2\text{C}(\text{OH})_2$ . The limiting potential for HER on this substrate is calculated to be -0.34 V, much more negative than on Cu metal catalyst (0.03 V).<sup>13</sup> We note that the experimental limiting potential of most HER active catalyst is usually -0.12 V or better.<sup>46</sup> Therefore, we believe that the HER activity of  $\text{Sc}_2\text{C}(\text{OH})_2$  is limited, which should lead to a more selective  $\text{CO}_2\text{RR}$  activity when compared with Cu metal.

We have also considered an alternative pathway for the formation of formic acid through the  $-\text{O}$  coordinated  $^*\text{OCHO}$  intermediate in Figure 1c. It can be seen that this pathway is less viable as the binding energy of this intermediate to the  $-\text{OH}$  terminated MXene is much stronger. Thus, a higher limiting potential for obtaining formic acid from the  $^*\text{OCHO}$  route of -1.13 V is predicted, which is much more negative than the limiting potential for  $\text{CH}_4$  formation. We note that such trend is fundamentally different from transition metal based catalyst such as Cu metal, where the limiting potential to formic acid *via*  $^*\text{OCHO}$  (-0.61 V) is less negative than the limiting potential  $\text{CH}_4$  formation (-0.74 V).<sup>13</sup> Even though  $^*\text{OCHO}$  can be stable from the aspect of thermodynamics, it is difficult for this intermediate to be further reduced into other intermediate due to the high limiting potential. Thus, it is likely that the  $^*\text{OCHO}$  will

revert to CO<sub>2</sub> following the reaction:



It should be noted that this process cannot increase the yield of H<sub>2</sub> for two reasons. Firstly, the  $\Delta G$  of this step (0.33 eV) is very similar to the  $-\text{OH} + \text{H}^+ + \text{e}^- \rightarrow -\text{O} + \text{H}_2$  step. Second, this process will occupy two active sites in MXene surface, compared to one in  $-\text{OH} + \text{H}^+ + \text{e}^- \rightarrow -\text{O} + \text{H}_2$  step. We believe that the side H<sub>2</sub> generation through  $*\text{OCHO}$  will actually suppress the overall HER in MXene. Therefore, we propose that Sc<sub>2</sub>C(OH)<sub>2</sub> MXene should be more suitable in catalyzing CO<sub>2</sub> to CH<sub>4</sub> than Cu metal.

The kinetic properties of Sc<sub>2</sub>C(OH)<sub>2</sub> also play a decisive role on the efficiency of CO<sub>2</sub>RR. Here, the climbing image-nudged elastic band (CI-NEB) simulation was carried out on the potential-limiting step:  $*(\text{H})\text{COOH} \rightarrow *\text{CO}$  in order to compute the activation barrier, which is the key parameter determining the overall reaction rate. The energy evolution profile for this potential-limiting step is shown as Figure 2d. The activation barrier is as low as 0.4 eV, suggesting an efficient CO<sub>2</sub>RR with high turnover rate. Therefore, Sc<sub>2</sub>C(OH)<sub>2</sub> can be expected to perform well on both aspects of low overpotential and low reaction barrier.

We have also computed the activation barrier for the  $*\text{CO} \rightarrow *(\text{H})\text{CHO}$  elementary step. Although this step is atypical, considering that CO<sub>2</sub>RR on most metallic catalysts has been predicted to go through either  $*\text{CHO}$  or  $*\text{COH}$  intermediate,<sup>13, 14, 47</sup> the activation barrier through  $*(\text{H})\text{CHO}$  is only 0.21 eV (Figure 2e), suggesting that the reaction can proceed very quickly without significant obstruction. The evolution of

transition states during the activation process (Figure 2e insets) also suggests that \*CHO (or \*COH) state is not involved in the CO<sub>2</sub>RR on –OH terminated MXene. The fact that \*CO intermediate on –OH terminated MXene can capture H atoms from solution and catalyst simultaneously means that the formation of \*CHO (or \*COH) is not required. This result further exhibits the advantage of MXenes on improving the catalytic efficiency due to less reaction steps and low activation energy barrier.

After establishing the distinct CO<sub>2</sub>RR pathways on –OH terminated MXenes, we proceeded to explore the scaling relations of the different intermediates on all 17 –OH terminated MXenes. In this work, the binding energy is calculated from the equation:

$$E_{bind,C_x(H)_a[H]_bH_yO_z} = E_{(slab-(a+b)H)+C_x(H)_a[H]_bH_yO_z} - [(E_{slab} - bE_{f,H}) + xE_{f,C} + yE_{f,H} + zE_{f,O}]$$

where  $E_{bind,C_x(H)_a[H]_bH_yO_z}$  represents the binding energy of a generic CO<sub>2</sub>RR intermediate with  $a$  and  $b$  representing the number of temporarily and permanently captured H atoms from substrate respectively. The binding energy is thus the difference between the energy of the intermediate-substrate complex and the sum of the energy of slab (perfect –OH terminated MXene), and the formation energies of C, H and O, minus  $b$  number of permanently captured [H]. The formation energies used in the equation are calculated from the linear combinations of H<sub>2</sub>, CO and H<sub>2</sub>O.

As the majority of the intermediates are coordinated to the substrate through the captured (H) atoms, we expect a different scaling relation on –OH terminated MXenes compared to transition metal catalysts, where most of the intermediates are bound to the substrate through –C coordination and have linearly-scaled binding strength.<sup>14, 15</sup> In

this regard, a more relevant metric is then how easily the (H) atoms can be captured from the  $T_x$  group. To describe this, the term  $E_{Hvac}$  is introduced:

$$E_{Hvac} = E_{slab-H} - (E_{slab} - E_{f,H})$$

where  $E_{slab-H}$  describes a defective MXene surface losing one (H) atom captured by an intermediate. A more negative  $E_{Hvac}$  indicates a more facile capture of (H) atom by the intermediate. Plotting the intermediate binding energy  $E_{bind,C_x(H)_a[H]_bH_yO_z}$  vs.  $E_{Hvac}$  reveals good linear relationships on most intermediates, which bind to the substrate through captured (H) (Figure 3). The only exception is \*CO; the lack of linearity between  $E_{bind,CO}$  and  $E_{Hvac}$  is understandable as it is not coordinated to the substrate through \*(H) and its formation does not involve the process of (H) capture. More importantly, the results confirm the different scaling relations that govern CO<sub>2</sub>RR on –OH terminated MXenes, potentially allowing MXenes to bypass the \*CO dependency that limits the CO<sub>2</sub>RR activity on transition metal catalysts.<sup>48</sup>

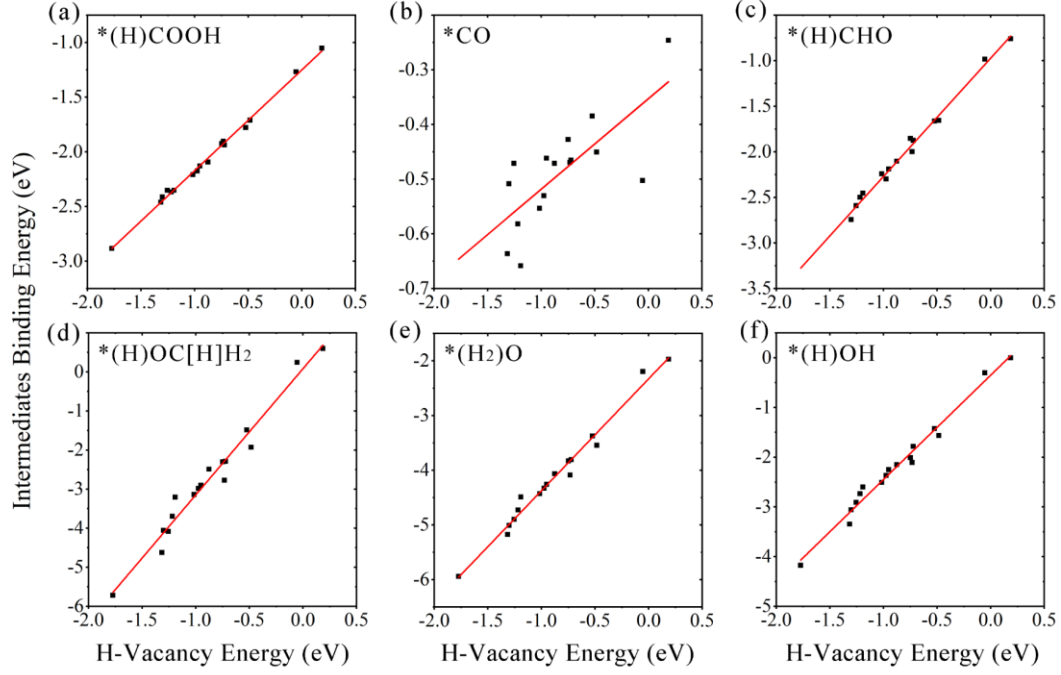


**Figure 3. Scaling relations for intermediates on OH-terminated MXenes.** Scaling relations for the electronic binding energies of (a)  $*(H)COOH$ , (b)  $*CO$ , (c)  $*(H)CHO$ , (d)  $*(H)OC[H]H_2$ , (e)  $*(H_2)O$ , (f)  $*(H)OH$  are plotted as a function of  $E_{Hvac}$ . More negative  $E_{Hvac}$  values indicate that the H in the MXene  $T_x$  is easier to be detached.  $*CO$  adsorption on  $Ta_2N(OH)_2$  ( $E_{Hvac} = -1.77$  eV), and  $*(H)CHO$  on  $Ta_2N(OH)_2$  and  $Nb_2N(OH)_2$  ( $E_{Hvac} = -1.31$  eV) were unstable ( $*CO$  will transform to  $*(H)C[H]O$  and  $*(H)CHO$  will transform to  $*(H)OC[H_2]H$  and omitted from (b) and (c).

After correcting for  $ZPE$ ,  $C_p$  and  $T \times S$  terms, we examine the dependence of the free energy variance on the  $E_{Hvac}$  during each elementary step. The limiting potentials ( $U_L$ ) of each elementary step is a linear function of  $E_{Hvac}$ , which can be expressed as:

$$U_L = U_0 + \alpha^{*H} \times E_{Hvac}$$

Here,  $U_0$  is the limiting potential when  $E_{Hvac} = 0$ .  $\alpha^{*H}$  is the slope that describes how much  $E_{Hvac}$  is impacting  $U_L$ . The specific values of  $U_0$  and  $\alpha^{*H}$  for each elementary step are listed in Table 1. We found that for the following four elementary steps of  $CO_2(g)$



$\rightarrow \text{*(H)COOH}$ ;  $\text{*CO} \rightarrow \text{*(H)CHO}$ ;  $\text{*(H)CHO} \rightarrow \text{*(H)OC[H]H}_2$ ; and  $\text{*(H)OC[H]H}_2 \rightarrow \text{*(H}_2\text{)O} + \text{C[H]H}_3(\text{g})$  the  $U_L$  becomes less negative with more negative  $E_{Hvac}$ . This trend indicates lower overpotential requirement (or higher activity) for these elementary steps when (H) on the substrates is easier to capture. For the rest of the elementary steps, the inverse relation between  $U_L$  and  $E_{Hvac}$  is observed.

**Table 1.** Specific values of coefficients for each elementary step along the lowest energy pathway of CO<sub>2</sub>RR on OH-terminated MXenes. (slab- $n$ H) represents the catalyst surface with  $n$  hydrogen vacancy.

No.	Reaction Steps	$U_0$ (eV)	$\alpha^{*H}$
1	$\text{CO}_2(\text{g}) + \text{slab} + \text{H}^+ + \text{e}^- \rightarrow \text{*(H)COOH} + (\text{slab-H})$	-0.073	-0.921
2	$\text{*(H)COOH} + \text{H}^+ + \text{e}^- + (\text{slab-H}) \rightarrow \text{*CO} + \text{H}_2\text{O}(\text{g}) + \text{slab}$	-0.650	0.703
3	$\text{*CO} + \text{H}^+ + \text{e}^- + \text{slab} \rightarrow \text{*(H)CHO} + (\text{slab-H})$	0.299	-1.081
4	$\text{*(H)CHO} + \text{H}^+ + \text{e}^- + (\text{slab-H}) \rightarrow \text{*(H)OC[H]H}_2 + (\text{slab-2H})$	0.952	-0.751
5	$\text{*(H)OC[H]H}_2 + \text{H}^+ + \text{e}^- + (\text{slab-2H}) \rightarrow \text{*(H}_2\text{)O} + \text{C[H]H}_3(\text{g}) + (\text{slab-3H})$	0.839	-1.180
6	$\text{*(H}_2\text{)O} + \text{H}^+ + \text{e}^- + (\text{slab-3H}) \rightarrow \text{*(H)OH} + (\text{slab-2H})$	0.202	1.132
7	$\text{*(H)OH} + \text{H}^+ + \text{e}^- + (\text{slab-2H}) \rightarrow \text{H}_2\text{O}(\text{g}) + (\text{slab-H})$	-0.091	1.099
8	$(\text{slab-H}) + \text{H}^+ + \text{e}^- \rightarrow \text{slab}$	-0.289	1.000

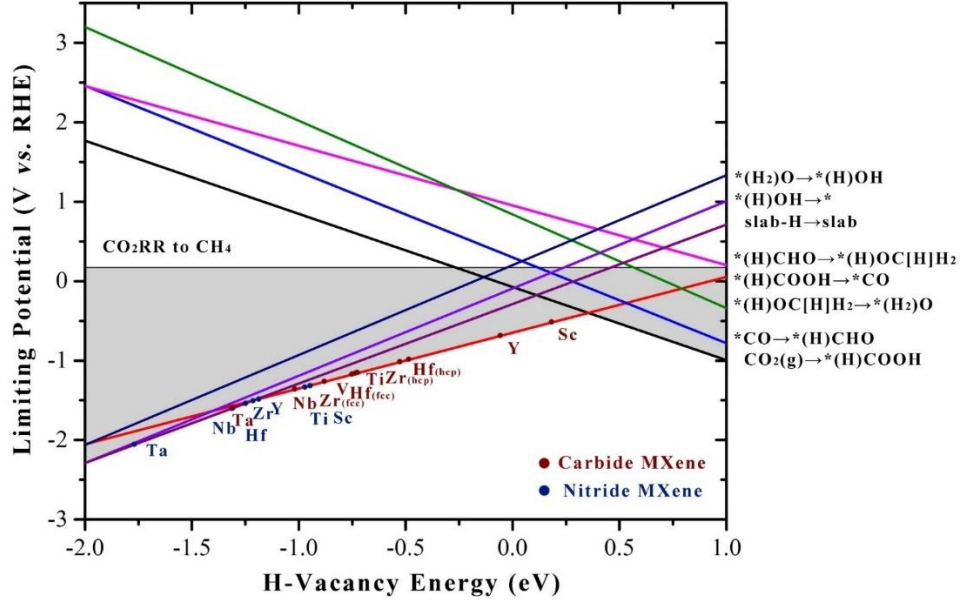


**Figure 4. Volcano curve of OH-terminated MXenes.** Each line represents an elementary step described on the right side. The potential-limiting step for each  $E_{Hvac}$  is then the elementary step represented by the bottom line with the most negative limiting potential. The different MXenes are marked with dots and arranged according to their  $E_{Hvac}$ . The equilibrium potential for CO<sub>2</sub>RR to CH<sub>4</sub> is 0.17 V vs. RHE.

Figure 4 shows the volcano curve, relating all 8 elementary steps to the  $E_{Hvac}$  for the –OH terminated MXenes in this study. As Hf<sub>2</sub>C(OH)<sub>2</sub> and Zr<sub>2</sub>C(OH)<sub>2</sub> have mixed terminations, the adsorptions on both surfaces exhibit different binding and thus they are omitted. Compared with the CO<sub>2</sub>RR volcano curve of transition metals,<sup>14</sup> the line that represents  $*CO \rightarrow *CHO$  is absent, while a new line representing the “[H] returning” (slab-H)  $\rightarrow$  slab step is introduced. Additionally, the  $U_0$  and  $\alpha^{*H}$  of some steps are different due to the captured (H) atom originating from the substrate. We note that for most OH-terminated MXenes, the potential-limiting step is determined to be  $*(H)COOH \rightarrow *CO$  (Figure 4). Sc<sub>2</sub>C(OH)<sub>2</sub> and Y<sub>2</sub>C(OH)<sub>2</sub> are singled out to be the most

promising CO<sub>2</sub>RR catalysts studied here due to their proximity to peak of the volcano curve.

Since the majority of CO<sub>2</sub>RR intermediates' binding energy exhibit a good linear relationship with  $E_{Hvac}$  (Figure 3), we propose that  $E_{Hvac}$  can be used as a primary descriptor to assess the CO<sub>2</sub>RR performance of MXenes. When the bond between H and O atom in the T<sub>x</sub> group is very weak (*i.e.* more negative  $E_{Hvac}$ ), CO<sub>2</sub>RR is difficult to progress, as the potential-limiting step  $*(H)COOH \rightarrow *CO$  involves the process of “returning” the captured (H) onto T<sub>x</sub>. On the other hand, if the H binds O atom in the T<sub>x</sub> too firmly (*i.e.* more positive  $E_{Hvac}$ ), the conversion of  $CO_2 \rightarrow *(H)COOH$  becomes the potential-limiting step as it involves capturing (H) from T<sub>x</sub> (Figure 4). This means, the most favorable  $U_L$  can be achieved by tuning  $E_{Hvac}$  to the point where the two elementary steps of  $*(H)COOH \rightarrow *CO$  and  $CO_2 \rightarrow *(H)COOH$  have the same  $U_L$  ( $E_{Hvac}$  around 0.36 eV at the apex of the volcano). Our results indicate that the  $E_{Hvac}$  values of all –OH terminated MXenes studied here lie on the left side of the apex (*i.e.* easy to capture (H)). The key characteristic that made the overall CO<sub>2</sub>RR  $U_L$  of Sc<sub>2</sub>C(OH)<sub>2</sub> the least negative among all MXenes studied here is the relatively strong H–O bonding in the T<sub>x</sub> group, making it easy to convert  $*(H)COOH$  to  $*CO$ . We note that the overall CO<sub>2</sub>RR  $U_L$  on Sc<sub>2</sub>C(OH)<sub>2</sub> (-0.53 V) is less negative than Cu metal (-0.93 V), and similar to Ti<sub>2</sub>CO<sub>2</sub> (-0.52 V), which has also been proposed to be active among the O-terminated MXenes.<sup>34, 38</sup>

**Table 2. Bader charge of  $*(H)COOH$  and  $*CO$  in different MXenes.**  $e_{C-COOH}$  represents the

charge of C ion of  $^*(\text{H})\text{COOH}$ ,  $e_{\text{C-CO}}$  represents the charge of C ion of  $^*\text{CO}$ .  $\Delta e$  represents the difference of the charge of C ion between  $^*(\text{H})\text{COOH}$  and  $^*\text{CO}$ . Negative values mean the ions gain electron compared with the isolated atom.

<b>System</b>	$e_{\text{C-COOH}}$	$e_{\text{C-CO}}$	$\Delta e$
$\text{Sc}_2\text{C}(\text{OH})_2$	-1.381	-1.023	0.357
$\text{Y}_2\text{C}(\text{OH})_2$	-1.379	-1.031	0.348
$\text{Hf}_2\text{C}(\text{OH})_2$ ( <i>hcp</i> )	-1.373	-0.869	0.504
$\text{Zr}_2\text{C}(\text{OH})_2$ ( <i>hcp</i> )	-1.351	-0.867	0.483
$\text{Ti}_2\text{C}(\text{OH})_2$	-1.361	-0.859	0.503
$\text{Hf}_2\text{C}(\text{OH})_2$ ( <i>fcc</i> )	-1.379	-0.822	0.557
$\text{V}_2\text{C}(\text{OH})_2$	-1.390	-0.863	0.526
$\text{Zr}_2\text{C}(\text{OH})_2$ ( <i>fcc</i> )	-1.406	-0.840	0.567
$\text{Ti}_2\text{N}(\text{OH})_2$	-1.380	-0.811	0.570
$\text{Sc}_2\text{N}(\text{OH})_2$	-1.368	-0.804	0.564
$\text{Nb}_2\text{C}(\text{OH})_2$	-1.383	-0.806	0.577
$\text{Y}_2\text{N}(\text{OH})_2$	-1.374	-0.834	0.540
$\text{Zr}_2\text{N}(\text{OH})_2$	-1.402	-0.833	0.569
$\text{Hf}_2\text{N}(\text{OH})_2$	-1.397	-0.741	0.656
$\text{Ta}_2\text{C}(\text{OH})_2$	-1.391	-0.686	0.704
$\text{Nb}_2\text{N}(\text{OH})_2$	-1.402	-0.682	0.720

To gain further insight on its potential and activation barrier at the atomic level, we

conducted Bader charge analyses, emphasizing on the  $^*(\text{H})\text{COOH} \rightarrow ^*\text{CO}$  potential-limiting step. The binding effect comes from the interaction between C inside the intermediate and the  $-\text{OH}$   $\text{T}_x$  group in MXenes, so we focus on the charge migration on the C atom. Here, we calculated the amount of on-site charges in C ions in both  $^*(\text{H})\text{COOH}$  ( $e_{\text{C-COOH}}$ ) and  $^*\text{CO}$  ( $e_{\text{C-CO}}$ ) group (compared to an isolated C atom), and evaluated the charge difference ( $\Delta e = e_{\text{C-COOH}} - e_{\text{C-CO}}$ ) between them. The magnitudes of these parameters are listed as Table 2 according to the position of the MXenes in the volcano curve in Figure 4. Since the chemical bonding is associated with the sharing or transfer of electrons between the participating atoms, the changes of the electrons (*i.e.* charge difference) can indicate the change of interaction. By comparing the values of  $\Delta e$  on the different MXenes, it can be clearly found that less charge transfer during this elementary step can generally result in less free energy change, leading to better catalytic performance. Both  $\text{Sc}_2\text{C}(\text{OH})_2$  and  $\text{Y}_2\text{C}(\text{OH})_2$  lead to  $\Delta e$  as small as  $\sim 0.35 e$ , while all the other MXenes induce much higher charge transfer (larger than  $0.5 e$ ). We believe that if the charge migration during the elementary step is small, the catalyst can bind the two intermediates equally well, resulting in a smooth transition. Therefore, the catalyst with less charge transfer during the elementary step exhibits higher catalytic activity.

## CONCLUSION

In summary, we studied the catalytic ability of various OH-terminated MXenes for  $\text{CO}_2\text{RR}$ .  $\text{Sc}_2\text{C}(\text{OH})_2$  and  $\text{Y}_2\text{C}(\text{OH})_2$  were found to be the most promising catalysts with

limiting potential of -0.53 and -0.61 V respectively, which is notably less negative than Cu metal. We found the H atom in –OH terminated MXenes to be active, assisting the CO<sub>2</sub>RR process in forming more stable structures with intermediates and lowering the overpotential. As most intermediates are bound to the substrate *via* \*(H), the scaling relations and volcano curves are different from CO<sub>2</sub>RR on transition metal catalysts. Binding energy analyses indicated that the best CO<sub>2</sub>RR activity is achieved when the formation of H vacancy  $E_{Hvac}$  is at the turning point (0.36 eV). Bader charge analysis showed that less charge transfer during the potential-limiting step can induce better catalytic performance. Our study demonstrates the CO<sub>2</sub>RR potential of –OH terminated MXenes, and at the same time, provides new insights on the surface functionalization effect of MXenes in electrocatalysis.

## **AUTHOR INFORMATION**

### **Corresponding Authors**

\*E-mail: qianfan@buaa.edu.cn

\*E-mail: sehzw@imre.a-star.edu.sg

### **Notes**

The authors declare no competing financial interest.

## **ASSOCIATED CONTENT**

### **Supporting Information**

Methods and Descriptions of simulation results. The Supporting Information is

available free of charge on the ACS Publications website.

## ACKNOWLEDGMENTS

Q.F.Z. was supported by National Key Research and Development Program of China (No. 2017YFB0702100), Beijing Natural Science Foundation (2192029) and Technology Foundation for Selected Overseas Chinese Scholar, Ministry of Human Resources and Social Security of China. Z.W.S. was supported by the Singapore National Research Foundation (NRF-NRFF2017-04). D. L. is supported by the European Regional Development Fund in the IT4Innovations national supercomputing center - path to exascale project, project number CZ.02.1.01/0.0/0.0/16\_013/0001791 within the Operational Programme Research, Development and Education, grant No. 17-27790S of the Czech Science Foundation, Mobility grant No. 8J18DE004 and SGS No. SP2019/110.

## REFERENCES

1. Inventory of U.S. Greenhouse Gas Emissions and Sinks: 1990–2017. United States Environmental Protection Agency: 2019.
2. Seh, Z. W.; Kibsgaard, J.; Dickens, C. F.; Chorkendorff, I.; Nørskov, J. K.; Jaramillo, T. F., Combining Theory and Experiment in Electrocatalysis: Insights into Materials Design. *Science* **2017**, 355 (6321), eaad4998.
3. Whipple, D. T.; Kenis, P. J. A., Prospects of CO<sub>2</sub> Utilization via Direct Heterogeneous Electrochemical Reduction. *J. Phys. Chem. Lett.* **2010**, 1 (24), 3451-

3458.

4. Handoko, A. D.; Wei, F.; Jenndy; Yeo, B. S.; Seh, Z. W., Understanding Heterogeneous Electrocatalytic Carbon Dioxide Reduction through Operando Techniques. *Nat. Catal.* **2018**, *1* (12), 922-934.
5. Koper, M. T., Structure Sensitivity and Nanoscale Effects in Electrocatalysis. *Nanoscale* **2011**, *3* (5), 2054-2073.
6. Steinmann, S. N.; Michel, C.; Schwiedernoch, R.; Sautet, P., Impacts of Electrode Potentials and Solvents on the Electroreduction of CO<sub>2</sub>: a Comparison of Theoretical Approaches. *Phys. Chem. Chem. Phys.* **2015**, *17* (21), 13949-13963.
7. Chen, Y.; Li, C. W.; Kanan, M. W., Aqueous CO<sub>2</sub> Reduction at Very Low Overpotential on Oxide-derived Au Nanoparticles. *J. Am. Chem. Soc.* **2012**, *134* (49), 19969-19972.
8. Lum, Y.; Kwon, Y.; Lobaccaro, P.; Chen, L.; Clark, E. L.; Bell, A. T.; Ager, J. W., Trace Levels of Copper in Carbon Materials Show Significant Electrochemical CO<sub>2</sub> Reduction Activity. *Acs Catal.* **2015**, *6* (1), 202-209.
9. Asadi, M.; Kim, K.; Liu, C.; Addepalli, A. V.; Abbasi, P.; Yasaei, P.; Phillips, P.; Behranginia, A.; Cerrato, J. M.; Haasch, R.; Zapol, P.; Kumar, B.; Klie, R. F.; Abiade, J.; Curtiss, L. A.; Salehi-Khojin, A., Nanostructured Transition Metal Dichalcogenide Electrocatalysts for CO<sub>2</sub> Reduction in Ionic Liquid. *Science* **2016**, *353* (6298), 467-470.
10. Liu, M.; Pang, Y.; Zhang, B.; De Luna, P.; Voznyy, O.; Xu, J.; Zheng, X.; Dinh, C. T.; Fan, F.; Cao, C.; Arquer, F. P. G. d.; Safaei, T. S.; Mepham, A.; Klinkova, A.; Kumacheva, E.; Filleter, T.; Sinton, D.; Kelley, S. O.; Sargent, E. H., Enhanced



Electrocatalytic CO<sub>2</sub> Reduction via Field-induced Reagent Concentration. *Nature* **2016**, 537 (7620), 382.

11. Zhu, D. D.; Liu, J. L.; Qiao, S. Z., Recent Advances in Inorganic Heterogeneous Electrocatalysts for Reduction of Carbon Dioxide. *Adv. Mater.* **2016**, 28 (18), 3423-3452.

12. Cheng, M.-J.; Clark, E. L.; Pham, H. H.; Bell, A. T.; Head-Gordon, M., Quantum Mechanical Screening of Single-atom Bimetallic Alloys for the Selective Reduction of CO<sub>2</sub> to C<sub>1</sub> Hydrocarbons. *Acs Catal.* **2016**, 6 (11), 7769-7777.

13. Peterson, A. A.; Abild-Pedersen, F.; Studt, F.; Rossmeisl, J.; Nørskov, J. K., How Copper Catalyzes the Electroreduction of Carbon Dioxide into Hydrocarbon Fuels. *Energy Environ. Sci.* **2010**, 3 (9), 1311-1315.

14. Shi, C.; Hansen, H. A.; Lausche, A. C.; Nørskov, J. K., Trends in Electrochemical CO<sub>2</sub> Reduction Activity for Open and Close-packed Metal Surfaces. *Phys. Chem. Chem. Phys.* **2014**, 16 (10), 4720-4727.

15. Liu, X.; Xiao, J.; Peng, H.; Hong, X.; Chan, K.; Nørskov, J. K. J. N. C., Understanding Trends in Electrochemical Carbon Dioxide Reduction Rates. **2017**, 8, 15438.

16. Kuhl, K. P.; Cave, E. R.; Abram, D. N.; Jaramillo, T. F., New Insights into the Electrochemical Reduction of Carbon Dioxide on Metallic Copper Surfaces. *Energy Environ. Sci.* **2012**, 5 (5), 7050-7059.

17. Chen, C. S.; Handoko, A. D.; Wan, J. H.; Ma, L.; Ren, D.; Yeo, B. S., Stable and Selective Electrochemical Reduction of Carbon Dioxide to Ethylene on Copper

Mesocrystals. *Catal. Sci. Technol.* **2015**, 5 (1), 161-168.

18. Goodpaster, J. D.; Bell, A. T.; Head-Gordon, M., Identification of Possible Pathways for C–C Bond Formation during Electrochemical Reduction of CO<sub>2</sub>: New Theoretical Insights from an Improved Electrochemical Model. *J. Phys. Chem. Lett.* **2016**, 7 (8), 1471-1477.

19. Dinh, C.-T.; Burdyny, T.; Kibria, M. G.; Seifitokaldani, A.; Gabardo, C. M.; de Arquer, F. P. G.; Kiani, A.; Edwards, J. P.; De Luna, P.; Bushuyev, O. S.; Zou, C.; Quintero-Bermudez, R.; Pang, Y.; Sinton, D.; Sargent, E. H., CO<sub>2</sub> Electroreduction to Ethylene via Hydroxide-mediated Copper Catalysis at an Abrupt Interface. *Science* **2018**, 360 (6390), 783-787.

20. Reske, R.; Duca, M.; Oezaslan, M.; Schouten, K. J. P.; Koper, M. T.; Strasser, P., Controlling Catalytic Selectivities during CO<sub>2</sub> Electroreduction on Thin Cu Metal Overlayers. *J. Phys. Chem. Lett.* **2013**, 4 (15), 2410-2413.

21. Li, Y.; Cui, F.; Ross, M. B.; Kim, D.; Sun, Y.; Yang, P., Structure-sensitive CO<sub>2</sub> Electroreduction to Hydrocarbons on Ultrathin 5-fold Twinned Copper Nanowires. *Nano Lett.* **2017**, 17 (2), 1312-1317.

22. Loiudice, A.; Lobaccaro, P.; Kamali, E. A.; Thao, T.; Huang, B. H.; Ager, J. W.; Buonsanti, R., Tailoring Copper Nanocrystals Towards C<sub>2</sub> Products in Electrochemical CO<sub>2</sub> Reduction. *Angew. Chem. Int. Ed.* **2016**, 55 (19), 5789-5792.

23. Hori, Y.; Murata, A.; Takahashi, R., Formation of Hydrocarbons in the Electrochemical Reduction of Carbon Dioxide at a Copper Electrode in Aqueous Solution. *J. Chem. Soc., Faraday Trans. 1* **1989**, 85 (8), 2309-2326.

24. Huang, Y.; Handoko, A. D.; Hirunsit, P.; Yeo, B. S., Electrochemical Reduction of CO<sub>2</sub> Using Copper Single-Crystal Surfaces: Effects of CO\* Coverage on the Selective Formation of Ethylene. *ACS Catal.* **2017**, 7 (3), 1749-1756.
25. Naguib, M.; Kurtoglu, M.; Presser, V.; Lu, J.; Niu, J.; Heon, M.; Hultman, L.; Gogotsi, Y.; Barsoum, M. W., Two-Dimensional Nanocrystals Produced by Exfoliation of Ti<sub>3</sub>AlC<sub>2</sub>. *Adv. Mater.* **2011**, 23 (37), 4248–4253.
26. Naguib, M.; Mashtalir, O.; Carle, J.; Presser, V.; Lu, J.; Hultman, L.; Gogotsi, Y.; Barsoum, M. W., Two-Dimensional Transition Metal Carbides. *ACS Nano* **2012**, 6 (2), 1322-1331.
27. Naguib, M.; Mochalin, V. N.; Barsoum, M. W.; Gogotsi, Y., 25<sup>th</sup> Anniversary Article: MXenes: A New Family of Two-Dimensional Materials. *Adv. Mater.* **2014**, 26 (7), 992-1005.
28. Fredrickson, K. D.; Anasori, B.; Seh, Z. W.; Gogotsi, Y.; Vojvodic, A., Effects of Applied Potential and Water Intercalation on the Surface Chemistry of Ti<sub>2</sub>C and Mo<sub>2</sub>C MXenes. *J. Phys. Chem. C* **2016**, 120 (50), 28432-28440.
29. Handoko, A. D.; Steinmann, S. N.; Seh, Z. W., Theory-guided Materials Design: Two-dimensional MXenes in Electro-and Photocatalysis. *Nanoscale Horiz.* **2019**.
30. Anasori, B.; Lukatskaya, M. R.; Gogotsi, Y., 2D Metal Carbides and Nitrides (MXenes) for Energy Storage. *Nat. Rev. Mater.* **2017**, 2, 16098.
31. Khazaei, M.; Ranjbar, A.; Arai, M.; Sasaki, T.; Yunoki, S. J. J. o. M. C. C., Electronic Properties and Applications of MXenes: a Theoretical Review. **2017**, 5 (10), 2488.

32. Liu, J.; Guo, C.; Vasileff, A.; Qiao, S., Nanostructured 2D Materials: Prospective Catalysts for Electrochemical CO<sub>2</sub> Reduction. *Small Methods* **2017**, *1* (1-2), 1600006.
33. Ling, C.; Shi, L.; Ouyang, Y.; Wang, J., Searching for Highly Active Catalysts for Hydrogen Evolution Reaction Based on O-Terminated MXenes through a Simple Descriptor. *Chem. Mater.* **2016**, *28* (24), 9026-9032.
34. Handoko, A. D.; Khoo, K. H.; Tan, T. L.; Jin, H.; Seh, Z. W., Establishing New Scaling Relations on Two-Dimensional MXenes for CO<sub>2</sub> Electroreduction. *J. Mater. Chem. A* **2018**, *6* (44), 21885-21890
35. Li, P.; Zhu, J.; Handoko, A. D.; Zhang, R.; Wang, H.; Legut, D.; Wen, X.; Fu, Z.; Seh, Z. W.; Zhang, Q., High-throughput Theoretical Optimization of the Hydrogen Evolution Reaction on MXenes by Transition Metal Modification. *J. Mater. Chem. A* **2018**, *6* (10), 4271-4278.
36. Handoko, A. D.; Fredrickson, K. D.; Anasori, B.; Convey, K. W.; Johnson, L. R.; Gogotsi, Y.; Vojvodic, A.; Seh, Z. W., Tuning the Basal Plane Functionalization of Two-Dimensional Metal Carbides (MXenes) To Control Hydrogen Evolution Activity. *ACS Appl. Energy Mater.* **2018**, *1* (1), 173-180.
37. Seh, Z. W.; Fredrickson, K. D.; Anasori, B.; Kibsgaard, J.; Strickler, A. L.; Lukatskaya, M. R.; Gogotsi, Y.; Jaramillo, T. F.; Vojvodic, A., Two-Dimensional Molybdenum Carbide (MXene) as an Efficient Electrocatalyst for Hydrogen Evolution. *ACS Energy Lett.* **2016**, *1* (3), 589-594.
38. Zhang, X.; Zhang, Z.; Li, J.; Zhao, X.; Wu, D.; Zhou, Z., Ti<sub>2</sub>CO<sub>2</sub> MXene: a Highly Active and Selective Photocatalyst for CO<sub>2</sub> Reduction. *J. Mater. Chem. A* **2017**, *5* (25),

12899-12903.

39. Li, N.; Chen, X.; Ong, W.-J.; MacFarlane, D. R.; Zhao, X.; Cheetham, A. K.; Sun, C., Understanding of Electrochemical Mechanisms for CO<sub>2</sub> Capture and Conversion into Hydrocarbon Fuels in Transition-Metal Carbides (MXenes). *ACS Nano* **2017**, *11* (11), 10825-10833.
40. Harris, K. J.; Bugnet, M.; Naguib, M.; Barsoum, M. W.; Goward, G. R., Direct Measurement of Surface Termination Groups and Their Connectivity in the 2D MXene V<sub>2</sub>CT<sub>x</sub> Using NMR Spectroscopy. *J. Phys. Chem. C* **2015**, *119* (24), 13713-13720.
41. Steinmann, S. N.; Michel, C.; Schwiedernoch, R.; Filhol, J. S.; Sautet, P., Modeling the HCOOH/CO<sub>2</sub> Electrocatalytic Reaction: When Details Are Key. *ChemPhysChem* **2015**, *16* (11), 2307-2311.
42. Nørskov, J. K.; Rossmeisl, J.; Logadottir, A.; Lindqvist, L.; Kitchin, J. R.; Bligaard, T.; Jónsson, H., Origin of the Overpotential for Oxygen Reduction at a Fuel-Cell Cathode. *J. Phys. Chem. B* **2004**, *108* (46), 17886-17892.
43. Cramer, C. J., *Essentials of Computational Chemistry: Theories and Models*. John Wiley & Sons: West Sussex, England, 2013.
44. Stoyanov, E. S.; Stoyanova, I. V.; Reed, C. A., The Structure of the Hydrogen Ion (H<sub>aq</sub><sup>+</sup>) in Water. *J. Am. Chem. Soc.* **2010**, *132* (5), 1484-1485.
45. Huan, T. N.; Andreiadis, E. S.; Heidkamp, J.; Simon, P.; Derat, E.; Cobo, S.; Royal, G.; Bergmann, A.; Strasser, P.; Dau, H.; Artero, V.; Fontecave, M., From Molecular Copper Complexes to Composite Electrocatalytic Materials for Selective Reduction of CO<sub>2</sub> to Formic Acid. *J. Mater. Chem. A* **2015**, *3* (7), 3901-3907.

